Evolution of hierarchical clustering in the CFHTLS-Wide since $z \sim 1$[*]

M. Wolk,[1]† H. J. McCracken,[1] S. Colombi,[1] J. N. Fry,[1,2] M. Kilbinger,[3] P. Hudelot,[1] Y. Mellier[1] and O. Ilbert[4]

[1] *Institut d'Astrophysique de Paris, UMR 7095, 98 bis Boulevard Arago, 75014 Paris, France*
[2] *Department of Physics, University of Florida, Gainesville FL 32611-8440, USA*
[3] *CEA Saclay, Service d'Astrophysique (SAp), Orme des Merisiers, Bât. 709, 91191 Gif-sur-Yvette, France*
[4] *Laboratoire d'Astrophysique de Marseille, UMR 7326, 38 rue Frédéric Joliot-Curie, 13388 Marseille cedex 13, France*

16 January 2013

ABSTRACT

We present measurements of higher order clustering of galaxies from the latest release of the Canada-France-Hawaii-Telescope Legacy Survey (CFHTLS) Wide. We construct a volume-limited sample of galaxies that contains more than one million galaxies in the redshift range $0.2 < z < 1$ distributed over the four independent fields of the CFHTLS. We use a counts in cells technique to measure the variance $\bar{\xi}_2$ and the hierarchical moments $S_n = \bar{\xi}_n/\bar{\xi}_2^{n-1}$ ($3 \leqslant n \leqslant 5$) as a function of redshift and angular scale. The robustness of our measurements if thoroughly tested, and the field-to-field scatter is in very good agreement with analytical predictions. At small scales, corresponding to the highly non-linear regime, we find a suggestion that the hierarchical moments increase with redshift. At large scales, corresponding to the weakly non-linear regime, measurements are fully consistent with perturbation theory predictions for standard ΛCDM cosmology with a simple linear bias.

Key words: large-scale structure of Universe – methods: statistical

1 INTRODUCTION

In our current paradigm, structures in the Universe originate from tiny density fluctuations emerging from a primordial Gaussian field after an early inflationary period. Gravitational instability in an homogeneous expanding Universe dominated by Cold Dark Matter indeed gives rise to the rich variety of structures seen today by hierarchical clustering. This picture has shown to be consistent with measurements of in million-galaxy surveys of the local Universe like the Sloan Digital Sky Survey (SDSS)[1] and 2dF (Colless et al.

2001); however, our knowledge of the evolution of the distribution of galaxies and its changing relationship with underlying dark matter density field remains incomplete.

On small scales, the evolution of the galaxy distribution strongly depends on the physical processes of galaxy formation, while on larger scales, both the initial power spectrum as well as to the global geometry of the Universe play an important role. Precise measurements of the galaxy distribution as a function of redshift and galaxy type therefore represents a fundamental tool in cosmology and the n-point correlation functions provide a particularly powerful method to characterise it.

The two-point correlation function (along with is Fourier transform the power spectrum) is the most widely used statistic (e.g. Peebles 1980; Baumgart & Fry 1991; Martínez 2009, for a general review on the subject) as it provides the most basic measure of galaxy clustering – the excess in the number of pairs of galaxies compared to a random distribution as function of angular scale. Nevertheless, the two-point correlation function represents a full description only in the case of a Gaussian distribution for which all higher-order connected moments vanish by definition. It is well known that the *actual* galaxy distribution is non-Gaussian (e.g. Fry & Peebles 1978; Sharp et al. 1984;

Szapudi et al. 1992; Bouchet et al. 1993; Gaztanaga 1994). Such a non-Gaussianity is already induced by nonlinear gravitational amplification of mass fluctuations, even if they originated from an initial Gaussian field (e.g. Peebles 1980; Fry 1984; Juszkiewicz et al. 1993; Bernardeau et al. 2002, and references therein). But it can also be present in initial conditions thereselves, from topological defects such as textures or cosmic strings (Kaiser & Stebbins 1984) or fluctuations coming from certain inflationary models (Guth 1981; Bartolo et al. 2004, and references therein). In addition, the process of galaxy formation results in a "biased" distribution of luminous matter with respect to the underlying dark matter, which adds another level of complexity in the non Gaussian nature of the process (e.g. Politzer & Wise 1984; Bardeen et al. 1986; Fry & Gaztanaga 1993; Mo & White 1996; Bernardeau et al. 2002, and references therein). For all these reasons, high order moments are required to obtain a full statistical description of the galaxy distribution.

In this paper we will use the method of counts in cells to investigate the evolution of the variance $\bar{\xi}_2$ and the hierarchical moments $S_n = \bar{\xi}_n/\bar{\xi}_2^{n-1}$ ($3 \leqslant n \leqslant 5$) of the galaxy distribution from $z \sim 1$ to present day. Until now, the majority of papers which have looked at these quantities have analysed large local-Universe redshift surveys; see Ross et al. (2006a, 2007) for the SDSS and Baugh et al. (2004); Croton et al. (2004, 2007) for the 2dFGRS. Furthermore, only a few measurements have been made in the literature of the redshift evolution of the hierarchical moments. For example, Szapudi et al. (2001) used a purely magnitude-limited catalogue of $\sim 710\,000$ galaxies with $I_{AB} < 24$ in a contiguous $4 \times 4\,\mathrm{deg}^2$ region. By assuming a redshift distribution for their sources, they found that a simple model for the time evolution of the bias was consistent with their measurements of the evolution of S_3 as a function of redshift. They concluded that these observations favoured models with Gaussian initial conditions and a small amount of biasing, which increases slowly with redshift. Using spectroscopic redshifts from the VVDS-Deep survey, Marinoni et al. (2008) reconstructed the three-dimensional fluctuation to $z \sim 1.5$ and measured the evolution of $\bar{\xi}$ and S_3 over the redshift redshift range $0.7 < z < 1$. They found that the redshift evolution in this interval is consistent with predictions of first- and second-order perturbation theory.

Measuring accurately the higher-order moments of the galaxy distribution requires both very large numbers of objects and also a precise control of systematic errors and reliable photometric calibration: no previous surveys have the required combination of depth and areal coverage to make reliable measurements from low redshift to $z \sim 1$ in large volume-limited sample of galaxies.

In this work, we use data from the Canada-France-Hawaii Telescope Legacy Survey (CFHTLS) which has a unique combination of depth, area and image quality, in addition to an excellent and highly precise photometric calibration.

The paper is organized as follows. In Sect. 2, we present our data set and the sample selection. In Sect. 3, we outline the techniques we use to estimate the galaxy clustering starting from the two-point correlation function and going to higher orders. The results are described and interpreted in Sect. 4. Conclusions are presented in Sect. 5.

Throughout the paper we use a flat ΛCDM cosmology ($\Omega_\mathrm{m} = 0.23$, $\Omega_\Lambda = 0.77$, $H_0 = 100h\,\mathrm{km\,s^{-1}\,Mpc^{-1}}$ and $\sigma_8 = 0.8$) with $h = 0.71$. All magnitudes are given in the AB system.

2 OBSERVATIONS, REDUCTIONS AND CATALOGUE PREPARATION

2.1 The Canada-France-Hawaii Telescope Legacy Survey

In this work, we use the seventh and final version of the Canada-France-Hawaii-Telescope Legacy survey (CFHTLS)[2]. The T0007 data release results in a major improvement of the absolute and internal photometric calibration of the CFHTLS. Since T0007 is a reprocessing of previous releases, the actual area covered by this release is almost identical to previous versions (some additional observations were added to fill gaps in the survey created by malfunctioning detectors).

The improved photometric calibration has been achieved by applying recipes adopted by the Supernova Legacy Survey (SNLS)(SNLS)[3] for the SNLS/Deep fields to both the Deep and Wide fields of the CFHTLS (for details, see Regnault et al. 2009). This improved photometric accuracy translates into improved photometric redshift precision and in a consistent photometric redshift calibration over the four disconnected patches of the CFHTLS Wide.

Complete documentation of the CFHTLS-T0007 release can be found at the CFHT[4] site. In summary, the CFHTLS-Wide is a five-band survey of intermediate depth. It consists of 171 MegaCam deep pointings (of $1\,\mathrm{deg}^2$ each) which, as a consequence of overlaps, consists of a total of $\sim 155\,\mathrm{deg}^2$ in four independent contiguous patches, reaching a 80% completeness limit in AB of $u^* = 25.2$, $g = 25.5$, $r = 25.0$, $i = 24.8$, $z = 23.9$ for point sources. The photometric catalogs we use here were constructed by running `SExtractor`[5] in "dual-image" mode on each CFHTLS tile, using the gri images to create a χ^2-squared detection image (see Szalay et al. 1999). The final merged catalogue is constructed by keeping objects with the best signal-to-noise from the multiple objects in the overlapping regions. Objects are selected using i-band `MAG_AUTO` total magnitudes Kron (1980) and object colours are measured using 3 arcsec aperture magnitudes.

After applying a magnitude cut at $i < 22.5$, the entire sample contains 2,710,739 galaxies. After masking, the fields have an effective area of

$$S_{\mathrm{eff},i} = 58.33,\quad 18.50,\quad 37.04,\quad 18.50\,\mathrm{deg}^2, \tag{1}$$

for fields W1, W2, W3, and W4 respectively, leading to a total area of $133\,\mathrm{deg}^2$.

2.2 Photometric redshift and absolute magnitude estimation

The photometric redshifts we use here have been provided as part of the CFHTLS-T0007 release. They are fully documented on the corresponding pages at the TERAPIX[6] site and the photometric redshift release documentation[7] describes in details how the photometric redshifts were computed following (Ilbert et al. 2006; Coupon et al. 2009, 2012).

The photometric redshifts are computed using the "Le Phare"[8] photometric redshift code which uses a standard template fitting procedure. These templates are redshifted and integrated through the transmission curves. The opacity of the intra-galactic medium (IGM) is accounted for and internal extinction can be added as a free parameter to each galaxy. The photometric redshifts are derived by comparing the modelled fluxes and the observed fluxes with a χ^2 merit function. In addition, a probability distribution function is associated to each photometric redshift.

The primary template sets used are the four observed spectra (Ell, Sbc, Scd, Irr) from Coleman et al. (1980) complemented with two observed starburst spectral energy distribution (SED) from Kinney et al. (1996). These templates have been optimised using the VVDS deep spectroscopic sample (Le Fèvre et al. 2005). Next, an automatic zero-point calibration has been carried out using spectroscopic redshifts present W1, W3 and W4 fields. For spectral type later than Sbc, a reddening $E(B-V) = 0$ to 0.35 using the Calzetti et al. (2000) extinction law is applied.

Although photometric redshifts were estimated to $i < 24$, we selected objects brighter than $i = 22.5$ to limit outliers (see Table 3 of Coupon et al. 2009). Star-galaxy separation is carried out using a joint selection taking into account the compactness of the object and the best-fitting templates.

Finally, using the photometric redshift, the associated best-fitting template and the observed apparent magnitude in a given band, one can directly measure the k-correction and the absolute magnitude in any rest-frame band. Since at high redshifts the k-correction depends strongly on the galaxy SED, it is the main source of systematic errors in determining absolute magnitudes. To minimise the $k-$correction uncertainties, we derive the rest-frame luminosity at a wavelength λ using the object's apparent magnitude closest to $\lambda(1+z)$ according to the redshift of the galaxy (the procedure is described in Appendix A of Ilbert et al. 2005). For this reason the bluest absolute magnitude selection takes full advantage of the complete observed magnitude set. However, as the u-band flux has potentially larger photometric errors, we use M_g-band magnitudes.

2.3 Sample selection

We select all galaxies with $i' < 22.5$ outside masked regions. At this magnitude, our photometric redshift samples are 100% complete, for all galaxy spectral types, and our photometric redshift errors are small compared to our redshift bin width in the redshift range $0 < z < 1$.
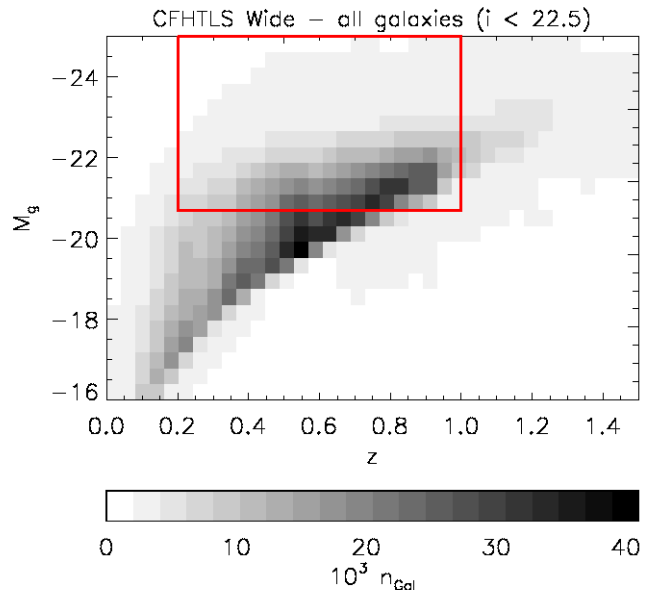
Figure 1. A two-dimensional histogram of the number density in the M_g-z plane is plotted for all galaxies in the CFHTLS wide, T0007 release. The red line shows our adopted thresholds in absolute luminosity and redshift.

Table 1. Number of galaxies per redshift bin outside the masked regions.

	W1	W2	W3	W4
$0.2 < z < 0.4$	36 307	12 121	23 426	10 945
$0.4 < z < 0.6$	100 586	31 586	67 413	32 778
$0.6 < z < 0.8$	165 215	48 596	105 020	59 137
$0.8 < z < 1.0$	149 960	45 783	96 737	52 423

Here we chose $M_g < -20.64$ ($M_g - 5\log h < -19.9$) and divide this selection into four redshift bins: $0.2 < z < 0.4$, $0.4 < z < 0.6$, $0.6 < z < 0.8$ and $0.8 < z < 1.0$. A large bin width ($\Delta z = 0.2$) ensures a low bin-to-bin contamination from random errors, but still reduces substantially the mixing of physical scales at a given angular scale that occurs in an angular catalog without redshift information.

The sample selection is illustrated in Figure 1. As a means of estimating the approximate completeness of our samples, we measured the mean absolute magnitude $\bar{M}_g$ in each of the redshift bins and found $\bar{M}_g = -21.4 \pm 0.1$. With this selection we have more than 10,000 objects in each bin in each Wide patch. The detailed number of objects in each sample is summarized in Table 1.

3 MEASURING GALAXY CLUSTERING

3.1 Two-point angular correlation function

As a consistency check with previous work, and as a means to verify our lower-order counts in cells moments, we measure the two-point angular correlation function $w(\theta)$ for our samples using the Landy & Szalay (1993) estimator,

$$w(\theta) = \frac{n_{\rm r}(n_{\rm r}-1)}{n_{\rm d}(n_{\rm d}-1)}\frac{DD}{RR} - \frac{n_{\rm r}-1}{n_{\rm d}}\frac{DR}{RR} + 1, \tag{2}$$

where, for a chosen bin from θ to $\theta + \delta\theta$, DD is the number of galaxy pairs of the catalog in the bin, RR the number of pairs of a random sample in the same bin, and DR the number of pairs in the bin between the catalog and the random sample. n_d and n_r are the number of galaxies and random objects respectively.

A random catalog is generated for each sample with the same geometry as the data catalog using $n_{\rm r} = 10^6$ which is at least 6 times and at the most 90 times $n_{\rm d}$ for a given bin and patch. We measure w in each field using the "`Athena`" tree code[9] in the angular range $\theta \in [0.001, 1]$ degrees divided into 15 bins spaced logarithmically.

In § 3.4 we explain how the individual measurements of $w(\theta)$ from the four different fields are combined.

3.2 Higher-order moments

Consider a distribution galaxy counts-in-cells which is a random sampling of a continuous underlying density field $\rho(\mathbf{r})$ where $\mathbf{r}$ is the coordinate of the object. The factorial moments of the number of galaxies in a set of random cells of size θ are closely related to the moments of the field through

$$F_k \equiv \langle N^{[k]} \rangle = \langle N(N-1)\cdots(N-k+1) \rangle = \bar{N}^k \bar{\rho}^k \tag{3}$$

where $\langle N^{[k]} \rangle$ represents the $k^{\rm th}$ factorial moment. $F_1 = \langle N \rangle = \bar{N}$ represents the average cell count and $\bar{\rho} = \rho \star W_\theta$ is the underlying density field smoothed with the window function of the cells.

The quantities of interest, however, are the hierarchical amplitudes S_k defined as

$$S_k = \frac{\bar{\xi}_k}{\bar{\xi}_2^{k-1}}, \tag{4}$$

where

$$\bar{\xi}_k = \frac{1}{V^k}\int_V \mathrm{d}\boldsymbol{r}_1 \ldots \mathrm{d}\boldsymbol{r}_k\, \xi_k(\boldsymbol{r}_1, \ldots, \boldsymbol{r}_k) \tag{5}$$

is the k-point correlation function averaged over the cell angular surface $V = s$ or volume $V = v$ according to whether statistics are considered in two or three dimensions, respectively. In particular,

$$\bar{\xi}_2 = \frac{1}{s^2}\int_s \mathrm{d}\theta_1\, \mathrm{d}\theta_2\, w(\theta_1, \theta_2). \tag{6}$$

The parameters S_3 and S_4, proportional to the skewness and the kurtosis of the distribution of the numbers of galaxies in cells, quantify deviations from the Gaussian limit. On a more general level, the hierarchical amplitudes S_k are expected to vary slowly with angular scale as a consequence of gravitational instability both in the weakly non-linear regime, as predicted by perturbation theory (Juszkiewicz et al. 1993; Bernardeau et al. 2002) and the highly non-linear regime as shown by Davis & Peebles (1977) by assuming stable clustering plus self-similarity (see also Peebles 1980; Bernardeau et al. 2002, and references therein).

To relate hierarchical moments to factorial moments one

[9] `http://www2.iap.fr/users/kilbinge/athena/`

can use the following recursion relation (Szapudi & Szalay 1993b; Colombi et al. 2000):

$$S_n = \frac{\bar{\xi}\,F_n}{N_{\rm c}^n} - \frac{1}{n}\sum_{k=1}^{n-1}\frac{n!}{(n-k)!\,k!}\,\frac{(n-k)\,S_{n-k}\,F_k}{N_{\rm c}^k} \tag{7}$$

with

$$\bar{\xi} \equiv \bar{\xi}_2 = F_2/F_1^2 - 1 \tag{8}$$

and $N_{\rm c} \equiv \bar{N}\bar{\xi}$.

In practice, one usually measures, for a cell of size θ, the count probability $P_N(\theta)$, the probability for a cell to contain N galaxies, as described below. Once $P_N(\theta)$ is measured, it is straightforward to calculate the factorial moments using

$$F_k \equiv \sum_N P_N N^{[k]}. \tag{9}$$

3.3 Measuring counts in cells

The main issue in counts in cells measurements is that large scales are dominated by edge effects (Szapudi & Colombi 1996; Colombi et al. 1998) due to the fact that, as cells have finite size, galaxies near the survey edges or near a masked region have smaller statistical weights than galaxies away from the edges. To correct for these defects, we use "BMW-P_N" (Black Magic Weighted P_N; Colombi & Szapudi 2012; Blaizot et al. 2006).

This method is based on the fact that counts in cells do not depend significantly on cell shape for a locally Poissonian point distribution. This latter approximation allows one to distort the cells near the edges of the catalog and near the masks in order to reduce as much as possible edge effects discussed above. In practice, the data and the masks are pixellated on a very fine grid. In this case, one can consider all the possible square cells of all possible sizes. For each of these cells, an effective size is given which corresponds to the area that is contained in the cell after subtraction of the masked pixels. If the fraction of masked pixels in the cell exceeds some threshold f, the cell is discarded. Then, the center of mass for the unmasked part of the cell is calculated and the algorithm finds the corresponding pixel it falls into. As one cell per pixel is enough to extract all the statistical information, the code selects among all the cells of equal unmasked volume targeting the same pixel the most compact one, i.e. the one which has been the least masked.

Note that the current implementation of BMW-P_N works only in the small angle approximation regime. This is not an issue in our analyses as the largest field W1 has an angular extension smaller than 9 degrees.

We used the following parameters in BMW-P_N: the sampling grid pixel size was set to 1.93 arcsec, which corresponds to a grid of size 16000×13944 for W1. This very high resolution allowed us to probe in detail the tails of the count in cells probability at scales as small as $\theta_{\rm min} = 0.0011\,\mathrm{deg}$. We measured counts in square cells of size θ for 15 angular scales, logarithmically spaced in the range $\theta \in [\theta_{\rm min}, \theta_{\rm max}]$ with $\theta_{\rm max} = 1\,\mathrm{deg}$ (see Tables B1).

The allowed fraction of masked pixels per cell f is a crucial parameter. If f is too large, the cells become too elongated, invalidating the local Poisson approximation. On other hand, if f is too small, edge effects become prominent.

We investigated the following set of values of f for W1 in the redshift bin $0.6 < z < 0.8$: $f = 0$, which corresponds to a traditional counts in cells measurement with square cells not overlapping with the edges of the catalog or the masks, and $f = 0.25, 0.5, 0.75$. We found that f as large as 0.5 is needed to ensure that edge effects are minimised in the scaling range probed by our measurements. Larger values of f do not change the results significantly so we kept $f = 0.5$ to reduce as much as possible cell shape anisotropies.

3.4 Combining fields

Factorial moments obtained from equation (9), where counts in cells are measured on a single field Wi, are unbiased estimators. However, concerning counts in cells, the quantities of interest are the averaged two-point correlation function $\bar{\xi}$ and the hierarchical moments S_n, which are non linear combinations of F_n, as in equations (7) and (8), and hence biased statistics (e.g. Szapudi et al. 1999). To minimise the bias, it is preferable to first perform a weighted average of the factorial moments over the four fields with weights proportional to effective area $S_{\text{eff},i}$,

$$\bar{F}_n = \frac{\sum_i S_{\text{eff},i} F_{n,i}}{\sum_i S_{\text{eff},i}}, \tag{10}$$

where $F_{n,i}$ is the nth factorial moment measured on field i and $S_{\text{eff},i}$ its effective area (equation 1) – and then, to use equations (7) and (8) to compute $\bar{\xi}$ and S_n from $\bar{F}_n$.

We have decided to use the same weighting procedure as in equation (10) to combine the individual correlation functions $w_i(\theta)$ measured in each field and derive a combined $w(\theta)$. This simpler approach leads to slightly biased measurements but is sufficient for our purpose.

To calculate error bars, we exploit the fact that we have at our disposal four independent fields to estimate statistical uncertainties directly from the data, using the dispersion among the four fields. The calculation of such errors is potentially complicated, as each field has a different area. For the factorial moments, which are unbiased, the errors are

$$(\Delta F_k)^2 = \frac{1}{(n_{\text{fields}} - 1)} \sum_i S_{\text{eff},i} (F_{k,i} - \bar{F}_k)^2 / \sum_i S_{\text{eff},i}. \tag{11}$$

Details are provided in Appendix A.

Rigorously speaking, a full error propagation formula should be used to compute the statistical uncertainties of $w(\theta)$ (Landy & Szalay 1993; Bernstein 1994), and of $\bar{\xi}$ and S_n (Szapudi et al. 1999). However in our case an involved procedure such as this is unnecessary since the uncertainties on the estimated errors are very large due to the fact that we have access to only four independent fields. To keep the approach simple while preserving, in practice, sufficient accuracy, we compute the errors on $w(\theta)$, $\bar{\xi}$ and S_n as for the F_k, by simply replacing $F_{k,i}$ with $w_i(\theta)$, $\bar{\xi}_i$ or $S_{k,i}$ in equation (11) (i is the field number), where the quantities $\bar{\xi}_i$ and $S_{k,i}$ are derived from $F_{k,i}$ using equations (7) and (8).

The hierarchical moments and their associated error bars are presented for each redshift bin in Tables B1.

3.5 Transformation to physical co-ordinates

Transformation to physical co-ordinates is treated following Groth & Peebles (1977) and Fry & Peebles (1978), originally due to Limber (1953). Let $\bar{n}$ be the spatial density of galaxies and ϕ be the selection function, that is, the probability that a galaxy at comoving distance x or redshift z is included in the catalog. Summed over distances in a spatially flat universe, the projected number density $\bar{\mathcal{N}}$ per solid angle in a given redshift range $z_{\min} < z < z_{\max}$ is

$$\bar{\mathcal{N}} = \int a^3 x^2 \mathrm{d}x \, \bar{n} \phi = \int_{z_{\min}}^{z_{\max}} n(z) \, \mathrm{d}z, \tag{12}$$

where a photon at redshift z arrives from comoving distance

$$x(z) = c H_0^{-1} \int_0^z \frac{\mathrm{d}z'}{\sqrt{\Omega_m (1 + z')^3 + \Omega_\Lambda}}. \tag{13}$$

The density of galaxies per solid angle per redshift interval is

$$n(z) = \frac{\mathrm{d}N}{\mathrm{d}z \, \mathrm{d}\Omega} = \bar{n} a^3 x^2 \frac{\mathrm{d}x}{\mathrm{d}z} \, \phi. \tag{14}$$

The factor $\bar{n} a^3$ is constant, and we take $a(z = 0) = 1$. Each sample has a characteristic depth weighted by geometry and redshift distribution,

$$x^* = \frac{\int n(z) \, x(z) \, \mathrm{d}z}{\int n(z) \, \mathrm{d}z}, \tag{15}$$

where the integrals run from $z_{\min}$ to $z_{\max}$. The angular density scales as $\bar{\mathcal{N}} \sim (x^*)^3$.

The projected two-point function $w(\theta)$ is related to the spatial two-point function $\xi(x)$ as

$$\bar{\mathcal{N}}^2 w(\theta) = \int n(z_1) \, \mathrm{d}z_1 \, n(z_2) \, \mathrm{d}z_2 \, \xi(x_{12}). \tag{16}$$

The correlation function is important only at small separations, for which x_{12} is

$$x_{12}^2 = \left(\frac{\mathrm{d}x}{\mathrm{d}z}\right)^2 \Delta z^2 + x^2 \, \Delta\theta^2. \tag{17}$$

Changing variables to $z = \frac{1}{2}(z_1 + z_2)$ and $\Delta z = z_1 - z_2$, and defining y as $y = (\mathrm{d}x/\mathrm{d}z)\Delta z/x\theta$ leads to

$$\bar{\mathcal{N}}^2 w(\theta) = \int \mathrm{d}z \, n^2(z) \int \frac{x \, \theta \, \mathrm{d}y}{\mathrm{d}x/\mathrm{d}z} \, \xi\big(x\theta(1 + y^2)^{1/2}\big). \tag{18}$$

To the extent that x^* is the characteristic scale for x, the second moment scales as $w(\theta) = x^{*-1} \, \mathrm{Fct}(\theta x^*)$; that is, the combination $x^* w$ is a function of θx^* (cf. Groth & Peebles 1977).

The projection depends on the form of the spatial correlation function. The observed correlation function is approximately a power law; including the stable clustering time dependence, $\xi = a^{3-\gamma}(x/x_0)^{-\gamma}$, we have

$$w(\theta) = C_\gamma \, \theta^{1-\gamma} \, x_0^\gamma \, \frac{\int \mathrm{d}z \, n(z)^2 \, a^{3-\gamma} \, x^{1-\gamma} \, (\mathrm{d}x/\mathrm{d}z)^{-1}}{\left[\int \mathrm{d}z \, n(z)\right]^2}, \tag{19}$$

where

$$C_\gamma = \int_{-\infty}^{\infty} \frac{\mathrm{d}y}{(1 + y^2)^{\gamma/2}} = \frac{\Gamma(\frac{1}{2}) \, \Gamma(\frac{\gamma - 1}{2})}{\Gamma(\frac{\gamma}{2})} \approx 3.67909, \tag{20}$$

approximated for $\gamma \approx 1.8$. Thus, the angular two-point function is also a power law,

z_1	z_2	x^* (Mpc)	$F_{\mathrm{p}}(3)$	$F_{\mathrm{p}}(4)$	$F_{\mathrm{p}}(5)$
0.2	0.4	1280	1.09	1.28	1.61
0.4	0.6	1910	1.02	1.06	1.12
0.6	0.8	2530	1.02	1.05	1.10
0.8	1.0	3010	1.09	1.25	1.46

$$w(\theta) = \frac{I_2}{I_1^2} \, x_0^\gamma \, \theta^{1-\gamma}, \tag{21}$$

with power index shifted by 1.

The projected n-point function is given by the extension of equation (16),

$$\bar{\mathcal{N}}^k w_n = \int n_1 \, \mathrm{d}z_1 \ldots n_k \, \mathrm{d}z_k \, \xi_n. \tag{22}$$

For hierarchical model where the n-point correlation function can be expressed as a sum over products of 2-point correlation functions: $\xi_n = \sum Q_k \, \xi_{ij}^{k-1}$ (sum over connected terms), where Q_k are the reduced amplitudes and $\xi_{ij} \equiv \xi_2(\mathbf{x_i}, \mathbf{x_j})$. After a change of variables to the average redshift and $k-1$ differences, the angular correlation function is also found to be hierarchical, with amplitude $q_k = Q_k F_{\mathrm{p}}(k)$,

$$F_{\mathrm{p}}(k) = \frac{I_k \, I_1^{k-2}}{I_2^{k-1}}, \tag{23}$$

$$I_k = C_\gamma^{k-1} \int n^k \, \mathrm{d}z \left(\frac{a^{3-\gamma} x^{1-\gamma}}{\mathrm{d}x/\mathrm{d}z} \right)^{k-1}. \tag{24}$$

Table 2 shows numerical results for the redshift distribution of the data with $\gamma = 1.8$. Variations from field to field are generally less than a percent. Changing γ by 10% affects the results by at most a few percents, and considering the perturbation theory time dependence $\xi(x) \sim D^2(z)$ instead of $a^{3-\gamma}$ by less than 1%.

3.6   Effect of photometric errors

In order to quantify the effect of the photometric errors on the values of the S_n, we investigate how important the variation is in the projection factors. To do so we use results from Coupon et al. (2009) who compute the photometric redshifts for the CFHTLS Wide T0004. They use a template-fitting method to compute photometric redshifts calibrated with a large catalog of 16,983 spectroscopic redshifts from the VVDS-F02, VVDS-F22, DEEP2 and the zCOSMOS surveys. Their method includes correction of systematic offsets, template adaptation, and the use of priors. Comparing with spectroscopic redshifts, they find a photometric dispersion in the wide fields of 0.037-0.039 and at $i' < 22.5$. We then take a dispersion $\Delta z = 0.038 \, (1 + z)$, and we get the numbers presented in Table 3 for x*, Fp_2, Fp_3, Fp_4, Fp_5. We see that the errors on the photometric redshifts introduce a very small difference in the projected numbers and we can consider that they are negligible comparing to the error that we get from the field to field variance.
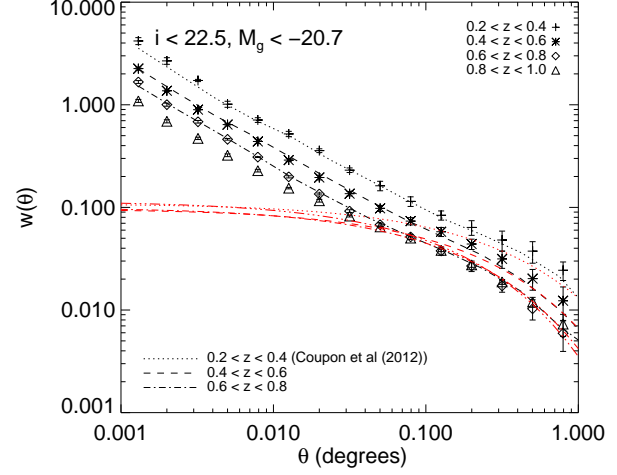
Figure 2. The two point angular correlation function, $w(\theta)$ (symbols) compared with the measurement of Coupon et al. (dotted, dashed and dot-dashed black curves). The red curves represents the linear theory prediction taking into account linear bias, as discussed in Section 4.2.3.

4   RESULTS

4.1   Two-point angular correlation function

As a first consistency check, Figure 2 shows our measurements of the two-point correlation function $w(\theta)$ in four redshift bins. We compare three bins with those of Coupon et al. (2012) (dashed lines). On the scales shown in this Figure, agreement between the two measurements is excellent. This is to be expected: at $i < 22.5$ the precision of photometric redshifts in CFHTLS release T0007 is similar to the previous release, T0006, used in Coupon et al. (2012). We over-plotted the dark matter predictions for the linear part of the two-point correlation function from which we determine the value of the bias in the different redshift bins. These are presented in Table 4. One can note that our values for the bias are close to unity do not strongly evolve with time.

Considering the average two point correlation (defined by equation 6) on Figure 3, we see, as expected, the same behaviour as $w(\theta)$ i.e that the clustering increases as the redshift decreases. We can also use this measurement to verify that the Landy & Szalay estimator measurements are consistent with BMW-PN measurements. To do this, we fit $w(\theta)$ by a simple power law $w = A\theta^{1-\gamma}$ using a χ^2 to estimate the amplitude A and the power γ. Our results are plotted on the left panel of Figure 3.

Using the formula 6 with square cells, we derive an approximate analytical expression for the average two point correlation function:

$$\bar{w} \sim \frac{4 \times 2^{(3-\gamma)/2}}{(3-\gamma)(4-\gamma)} \, A\theta^{1-\gamma}. \tag{25}$$

Comparing with a numerical integration, we found that this formula works for γ in the range [1.6, 2.0] (our values of γ are 1.9, 1.8, 1.7 and 1.65 for the redshift bins $0.2 < z < 0.4$, $0.4 < z < 0.6$, $0.6 < z < 0.8$ and $0.8 < z < 1.0$ respectively) with a precision that increases with γ. The differences in $\bar{w}$

z_1	z_2	x^* (Mpc)	$F_{\mathrm{p}}(3)$	$F_{\mathrm{p}}(4)$	$F_{\mathrm{p}}(5)$
0.2	0.4	1272	1.09	1.29	1.64
0.4	0.6	1905	1.02	1.07	1.14
0.6	0.8	2530	1.02	1.06	1.11
0.8	1.0	3005	1.09	1.25	1.48

Table 3. Projection parameters obtained using photometric redshifts and the dispersion in the estimated redshift of $\Delta z = 0.038\,(1+z)$. Columns give the redshift range, scaling distance and n-point amplitude projection factors $F_{\mathrm{p}}(n)$ (eq. [23]) for $n = 3, 4, 5$.
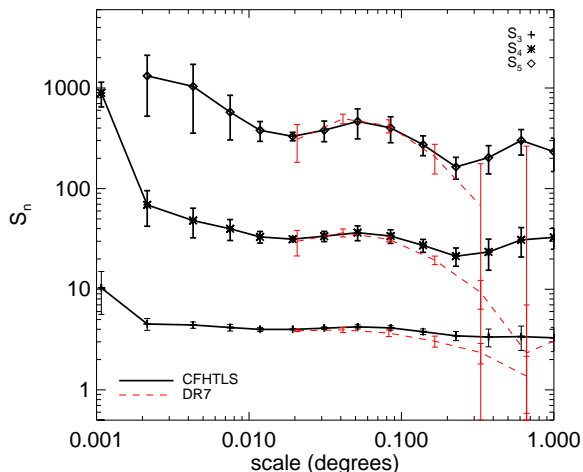
Figure 4. Hierarchical moments S_3, S_4 and S_5 measured in the DR7 release of the SDSS for galaxies selected with $0 < z < 0.4$, $18 < r < 21$ and $M_r < -20.7$ (dashed lines) compared to measurements in the CFHTLS (solid lines).

between the two methods ranges from 8.5% for $\gamma = 1.6$ to less than 1% for $\gamma = 2$. The results are presented on the right panel of Figure 3. We can see that this prediction matches very well the measurements.

4.2 Higher-order moments

4.2.1 Comparison with SDSS DR7

We now consider our measurements of the hierarchical moments. As first consistency check, we compare our S_ns measured in the CFHTLS to measurements made from the seventh data release of the Sloan Digital Sky Survey (SDSS-DR7) using an independently-written counts-in-cells code Ross et al. (2007). This code was used with the default configuration parameters proposed by the authors.

Since the SDSS and CFHTLS are by their nature very different surveys, we can only make this comparison for the lowest redshift bins in the CFHTLS. We therefore chose galaxies with $0 < z < 0.4$, $18 < r < 21$ and $M_r < -20.7$ (comparable to Ross et al. 2007) and applied the same selection to galaxies in the SDSS. Our results are plotted in Figure 4, where we show the hierarchical moments obtained from the four fields of the CFHTLS (solid lines) compared to measurements in the SDSS (dashed lines). For the CFHTLS, error bars are computed according to the method described in § 3.4; for the SDSS, error bars were computed using a

jackknife method (e.g., Scranton et al. 2002). For the detailed method see Ross et al. (2006b).

As a consequence of the extremely fine pixelisation grid we employ, we are able to measure our S_n to much smaller angular scales than in the SDSS (such a measurement would be computationally demanding for a large-area survey like the SDSS). In the common angular range, the agreement between the CFHTLS and the SDSS measurements is excellent except at the largest scales. In this latter regime, however, our measurements are expected to be less precise, due to finite size effects when approaching the angular size of the fields.

4.2.2 Field-to-field variations

Figure 5 shows the third-order cumulant S_3 as a function of scale in different redshift bins for the four different fields. At low redshifts, $z \lesssim 0.6$, the dispersion between the four fields is low; however, above $z \simeq 0.7$ W3 begins to be systematically higher than the other fields at all scales. At the highest redshifts, the difference between W3 and the other fields is significant. The same behaviour is observed for the other cumulants. To illustrate furthermore this point Figure 6 compares the hierarchical moments as a function of scale for the various redshift bins for the cases when all the fields are combined together and when W3 is excluded. The presence of W3 is in fact crucial because when it is included there clearly seems to be a redshift evolution of the hierarchical moments as indicated by the left panel of Figure 5, while removing W3 makes the redshift dependence insignificant as shown on the right panel. We now investigate this effect in more detail.

The explanation of the behavior of the cumulants at the highest redshift bin can be understood from an examination of Figure 7, which shows the counts in cells distribution function for the combined fields, W1+W2+W3+W4, for W1+W2+W4, and for W3 alone. Clearly, the presence of W3 dominates and perturbs considerably the high end tail of $P_N(\theta)$. A careful inspection of the W3 field reveals that this is due to the presence of one or several rich clusters in W3 compared to the three other fields (see e.g. Colombi et al. 1994). Due to the finiteness of the sample there is a value $N_{\max}(\theta)$, above which $P_N(\theta)$ becomes zero. This function $N_{\max}(\theta)$ obviously relates to the richest clusters of the sample: for instance a cell of size θ located in the densest part of one of the richest cluster of the sample should contain $N_{\max}(\theta)$ galaxies. Similarly, $P_N(\theta)$ for N close to $N_{\max}$ is entirely determined for a given smoothing scale θ by the density profile of a rich cluster of galaxies (cf. Figure 5 of Colombi et al. 1994).

To illustrate furthermore this point, Figure 8 shows the
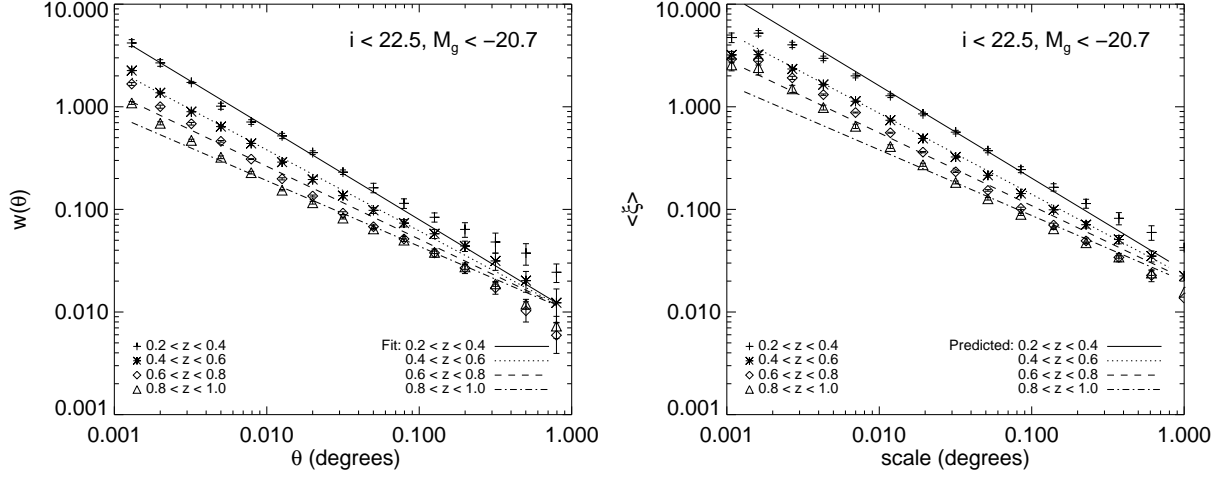
Figure 3. The symbols on the left panel represent the measurements of $w(\theta)$ in the four redshift bins. The lines are the fits obtained using a χ^2 assuming a power law for the two point correlation function. The symbols on the right panel show the averaged two point correlation measured using counts in cells. The lines are the predicted values using formula (31) with the parameters of our $w(\theta)$ fit.

largest cluster in W3 at $0.8 < z < 1.0$ [10] and the effect on S_3 of subtracting it from the field. As expected, removing the cluster greatly reduces the skewness over a large angular range. Indeed, moments of order k of the count probability are increasingly sensitive to the high-N tail of $P_N(\theta)$ with increasing k. Removing the largest cluster reduces the high N tail of $P_N(\theta)$ and hence reduces the skewness. This happens here only on a finite range of angular scales because, at smaller (larger) scales, one or several clusters with different concentration parameters from those of the one we selected dominate the high N tail of the count probability. In fact, detailed examination of the four fields in the redshift bin $0.8 < z < 1$ shows that there are four rich clusters in W3 and one in W1, which affect the cumulants and explains the discrepancy between W3 and the other fields.

4.2.3 Significance of field-to-field variations

To test if the discrepancy between W3 and the three other fields is statistically significant we decided to compute the theoretical expectation of the errors on $\bar{\xi}$, S_3 and S_4 in order to compare them to the errors estimated as described in § 3.4 and as shown in Table B1. This is made possible by the use of the package FORCE (FORtran for Cosmic Errors, Colombi & Szapudi 2001) which exploits the analytical calculations of Szapudi & Colombi (1996) and Szapudi et al. (1999) to provide quantitative estimates of these statistical errors due to the finiteness of the sample, given a number of input parameters that specify a prior model.

All the parameters needed for such a calculation were estimated from the survey self-consistently. These are the area S of the survey, the cell area s, the average galaxy number count $\bar{N}$, the averaged two-point correlation function over a cell $\bar{\xi}$, the values of S_n's for $3 \leqslant n \leqslant 8$ and the averaged two-point correlation function over the survey,

Redshift bin	b
$0.2 < z < 0.4$	1.17
$0.4 < z < 0.6$	1.21
$0.6 < z < 0.8$	1.27
$0.8 < z < 1.0$	1.37

Table 4. Bias in the different redshift bins.

$$\bar{\xi}_S = \frac{1}{S^2} \int_S \mathrm{d}\theta_1 \, \mathrm{d}\theta_2 \, w(\theta_1, \theta_2). \tag{26}$$

Except for $\bar{\xi}_S$, all the parameters above can be extracted directly from the data, including S_n, which measured up to the eighth order.

The calculation of $\bar{\xi}_S$ is however more complex. To perform it we use linear perturbation theory to derive a three-dimensional correlation function for a ΛCDM model. Then, we compute the angular two point correlation function in the various redshift bins using equation (16), from which we can derive numerically the integral (26).[11] The result is multiplied with the square of the bias between the galaxy and the dark matter distributions. To estimate this linear bias, we fit the measured two-point correlation function using the "halo-model" (Scoccimarro et al. 2001; Ma & Fry 2000; Peacock & Smith 2000; Cooray & Sheth 2002), exactly as in Coupon et al. (2012).[12] The values are given in Table 4.2.3.

Figure 9 compares the theoretical errors on $\bar{\xi}$, S_3 and S_4 derived with FORCE to the measured ones using the dispersion from the four fields. Three models are considered, as detailed in the caption of the figure, to reflect uncertainties on the theory. These theoretical predictions are expected to be valid only when relative errors are small compared to

---

[10] this cluster has coordinates $(216.5, 55.9)$ in radec J2000.

[11] $w(\theta)$ was computed using the halo-model module of COSMOPMC (http://cosmopmc.info), while $\bar{\xi}_S$ was estimated by Monte-Carlo simulation using 10^6 pairs to perform the integral.
[12] using again COSMOPMC.
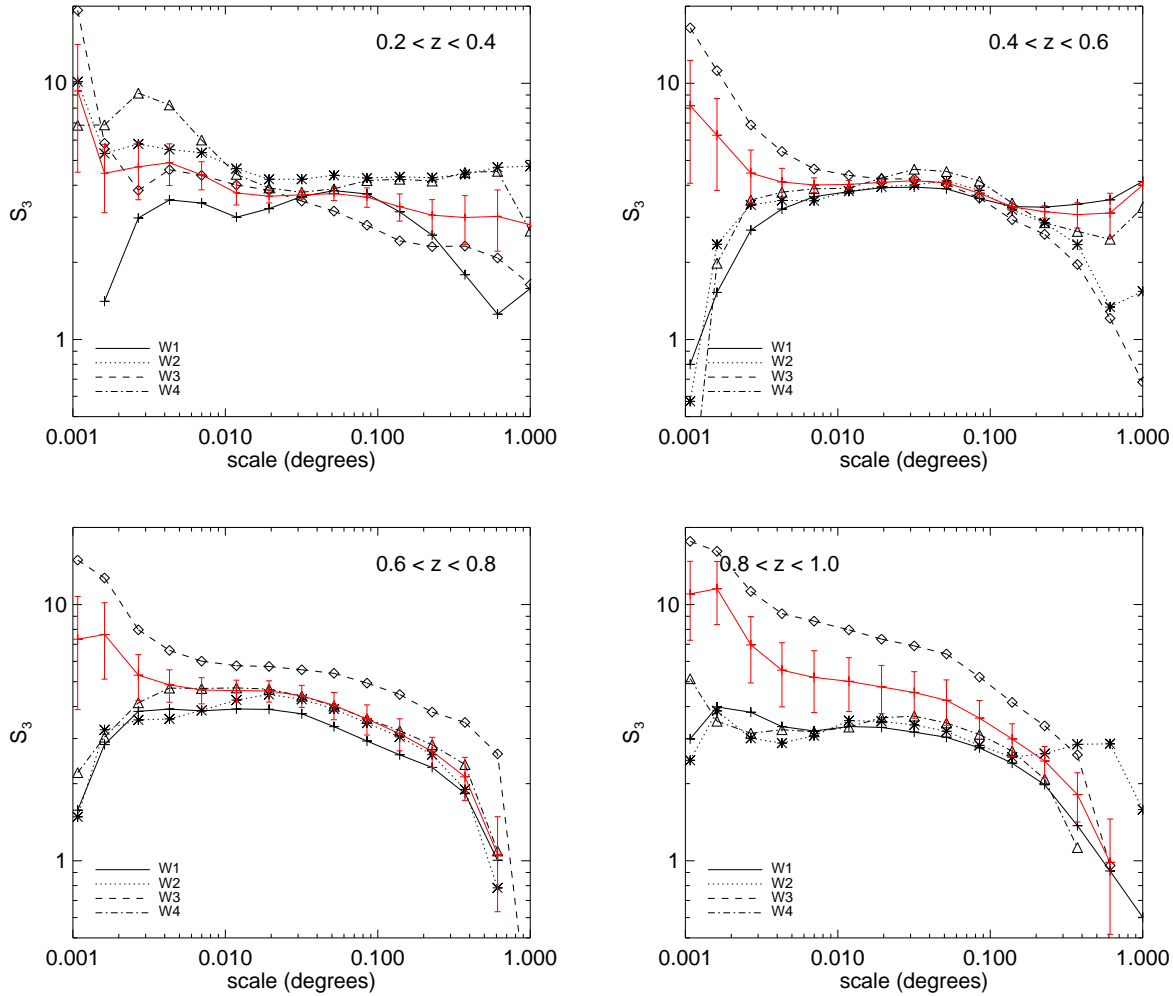
Figure 5. The four panels represent measurements of S_3 in the four fields of the CFHTLS from the lowest redshift bin $0.2 < z < 0.4$ to the highest one $0.8 < z < 1.0$. The red line represents the combined S_3 computed using the method described in Section 3.4. We can see that at low redshift all the fields behave identically while at higher z, S_3 in W3 is systematically higher over the whole scale range.

unity as consequence of the propagation error technique used to derive it. Consequently, predictions at scales beyond 0.1 degrees, where edge effects start to dominate in the theory are expected to be less accurate. With all these limitations in mind, one can see that the agreement between theory and measurements is excellent except in the redshift bin $0.6 < z < 0.8$ where the relative error seems to be slightly underestimated/overestimated by the measurements when comparing to the theory for $\bar{\xi}$ and the hierarchical moments respectively.

The remarkable agreement between theoretical errors derived using the standard ΛCDM model and the measured weighted dispersion between the four fields in the redshift bin $0.8 < z < 1$ demonstrates that in fact W3 *is not special*, from the statistical point of view. This is confirmed by the examination of Figure 10, which shows the hierarchical moments as functions of redshift for two typical angular scales: $\theta = 0.012\,\mathrm{deg}$, which corresponds in practice to the non-linear regime, and $\theta = 0.22\,\mathrm{deg}$, which is the largest possible

reliable scale in order to probe the weakly non linear regime. On this plot, one sees that the S_n measured after removing W3 are compatible within 2σ with those obtained with all the fields.

4.2.4 Evolution with redshift and comparison with perturbation theory

We have demonstrated that W3 does not represent a "special event" and that measurements with and without W3 are compatible within 2σ. This demonstrates that the redshift evolution trend in the non-linear regime observed on left panel of Figure 6 and on Figure 10 is indicative but inconclusive; this statement holds when angular scales are converted to Mpc. From now on, we do not consider furthermore W3 separately and present results only for the full combination of the four fields.

Figure 11 shows the hierarchical moments in three dimensional space as functions of physical scale after applying
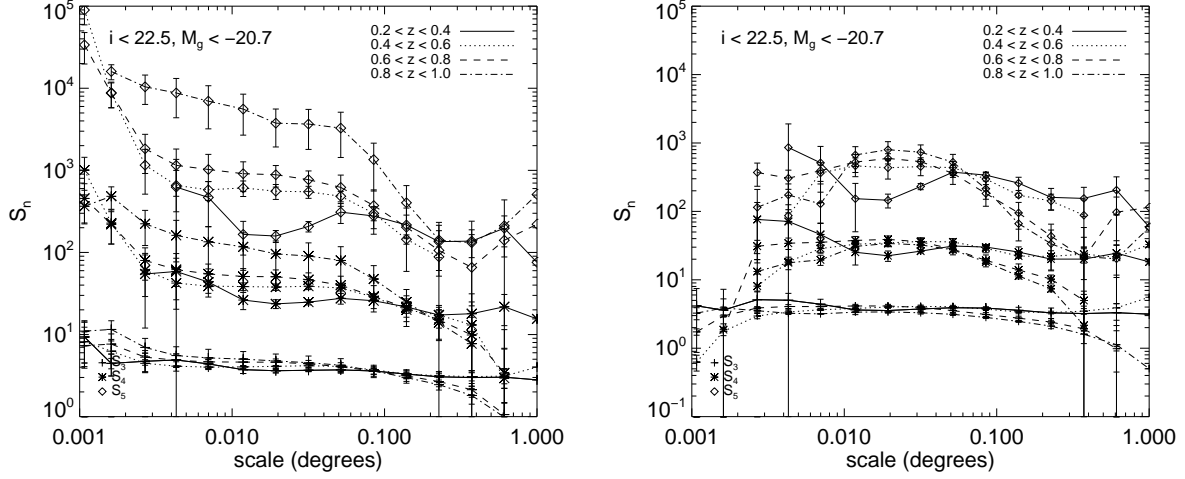
Figure 6. Combined S_n's as functions of angular scale in the four redshift bins when using W1+W2+W3+W4 together (left panel) and when W3 is excluded (right panel). Points which are not plotted correspond to negative values.
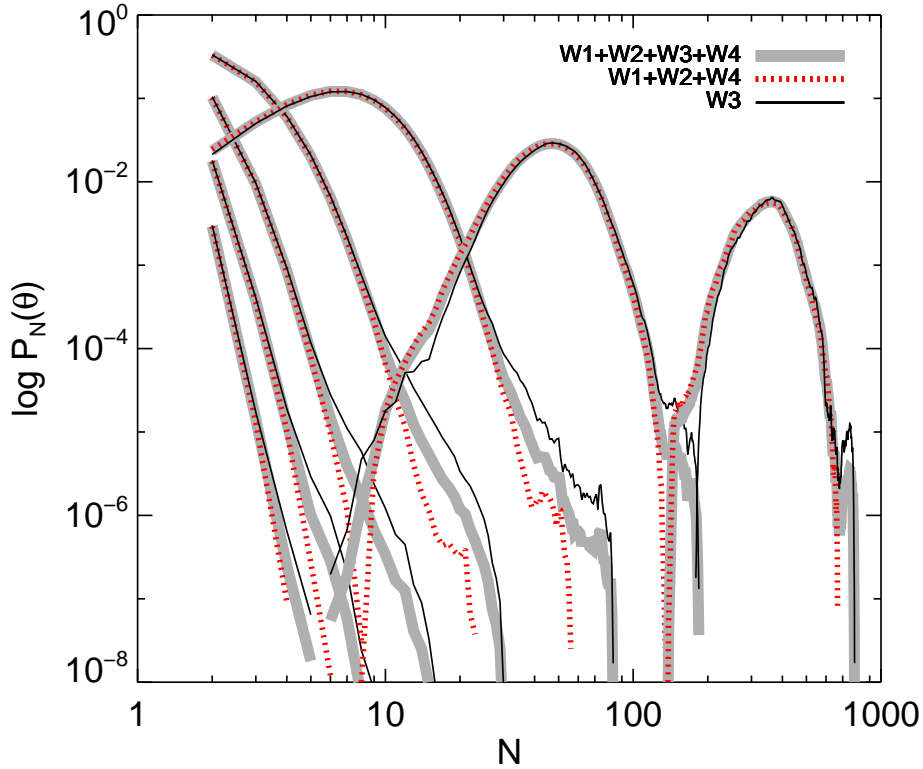
Figure 7. Counts in cells distribution function $P_N(\theta)$ as a function of N in the last redshift bin $0.8 < z < 1.0$. Three cases are considered: the combination W1+W2+W3+W4 using the weighting scheme as in equation (10) (thick grey curves), the combination W1+W2+W4 (red dotted curves) and W3 alone (solid black curves). Each curve corresponds to a different scale; for clarity we keep only one scale out of two.
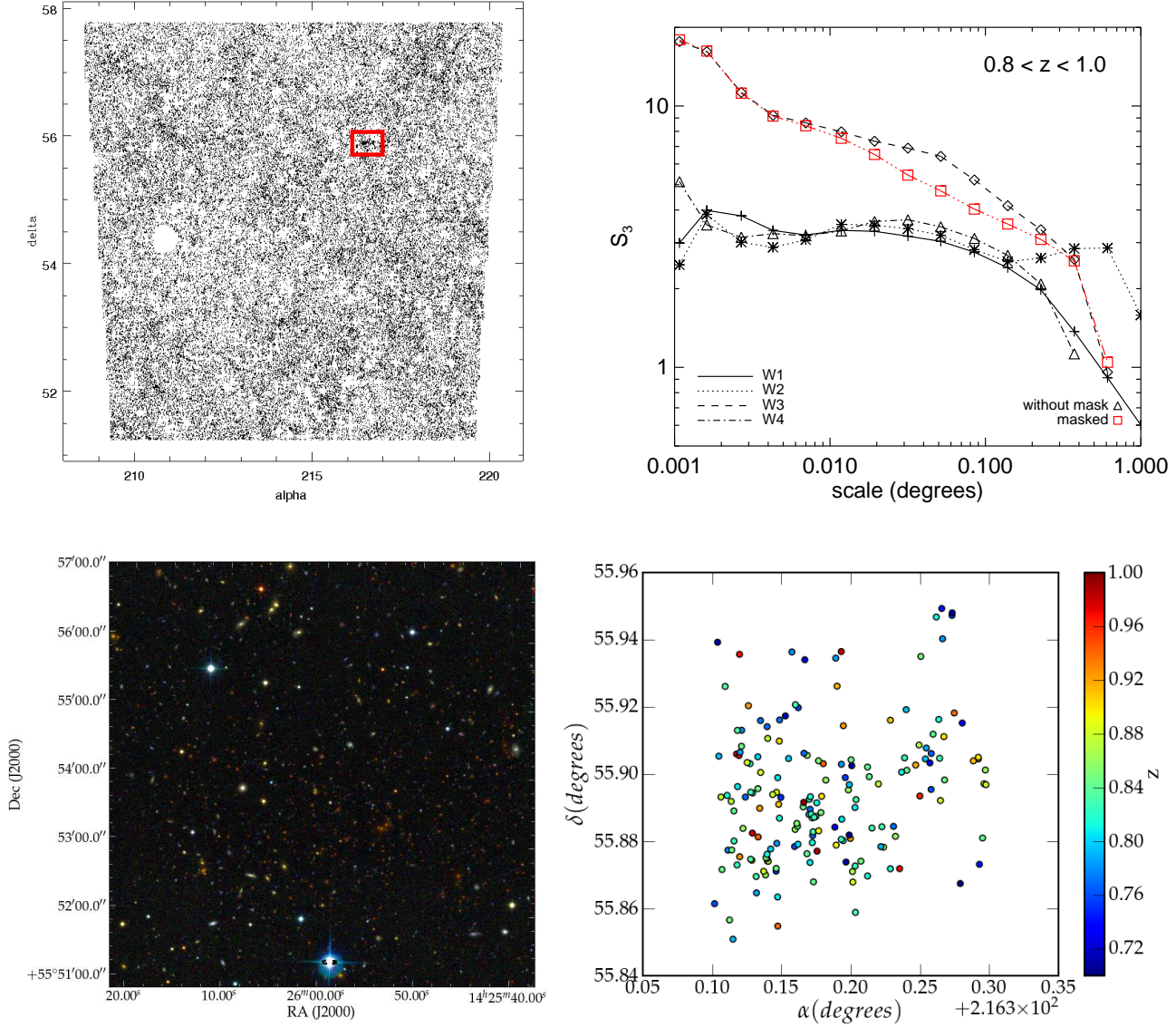
Figure 8. A rich cluster in W3. The upper left panel represents the distribution on the sky of galaxies in W3 for $0.8 < z < 1$. The red square encloses the most prominent concentration from a visual inspection. The upper right panel illustrates the effect of masking this concentration on S_3 for W3 in the highest redshift bin. The lower left panel shows a coloured image of the sky in the region delimited by the red square, which reveals a cluster of red galaxies. On the lower right panel, the galaxies of the same region are represented in the same field with symbol colour representing redshift. We use a wider redshift bin ($0.7 < z < 1.0$) to be sure not to cut galaxies that belong to the cluster due to photometric redshift errors.

the transformation described in Section 3.5. The measurements show the same behavior as before i.e. a plateau at small scales corresponding to the highly non-linear regime, and then tend to another lower plateau at large scales corresponding to the weakly non-linear regime. At scales ~ 10 Mpc, we start to be sensitive to finite size effects as we approach the size of the fields.

We now compare the measurements directly to perturbation theory predictions (Juszkiewicz et al. 1993; Bernardeau 1994a,b; Bernardeau et al. 2002):

$$S_3^{\mathrm{PT}} = \frac{34}{7} + \gamma_1, \tag{27}$$

$$S_4^{\mathrm{PT}} = \frac{60712}{1323} + \frac{62}{3}\gamma_1 + \frac{7}{3}\gamma_1^2 + \frac{2}{3}\gamma_2, \tag{28}$$

$$
\begin{aligned}
S_5^{\mathrm{PT}} = {} & \frac{200575880}{305613} + \frac{1847200}{3969}\gamma_1 + \frac{6940}{63}\gamma_1^2 \\
& + \frac{235}{27}\gamma_1^3 + \frac{1490}{63}\gamma_2 + \frac{50}{9}\gamma_1\gamma_2 + \frac{10}{27}\gamma_3
\end{aligned}
\tag{29}
$$

with $\gamma_p = \mathrm{d}^p \ln \sigma^2(R)/\mathrm{d}^p \ln R$, where $\sigma^2(R)$ is the linear variance of the 3D matter density field smoothed with a spherical top-hat window of radius R.

The agreement between perturbation theory predictions and the measurements at large scales is excellent and even better in a striking way, as it can be seen on in Figures 10
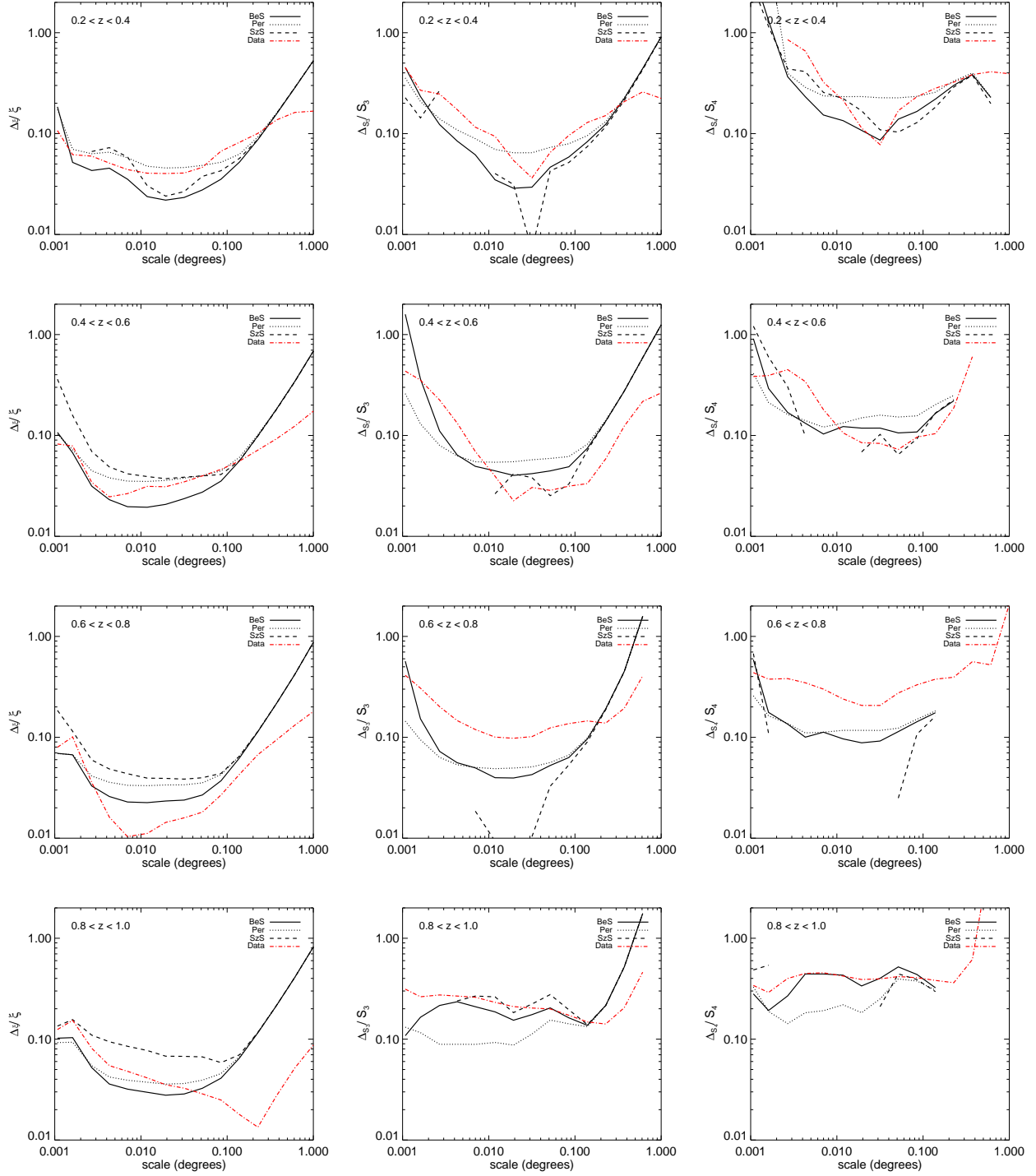
**Figure 9.** Comparison of theoretical errors to measured ones. The different panels from the left to the right represent the relative error on respectively the averaged two-point correlation function, S_3 and S_4 comparing the different models available in FORCE (black curves) to the errors measured from the dispersion over the four fields as explained in Section 3.4 (red curve). For the theoretical predictions, three different models are available, SzS from Szapudi & Szalay (1993a,b), BeS from Bernardeau & Schaeffer (1992) and Per uses perturbation theory predictions of Bernardeau (1994a, 1996). Each row of panels represents a different redshift bin going from the lowest one on the top to the highest one on the bottom. Some curves are interrupted where the models fail and give negative error bars.
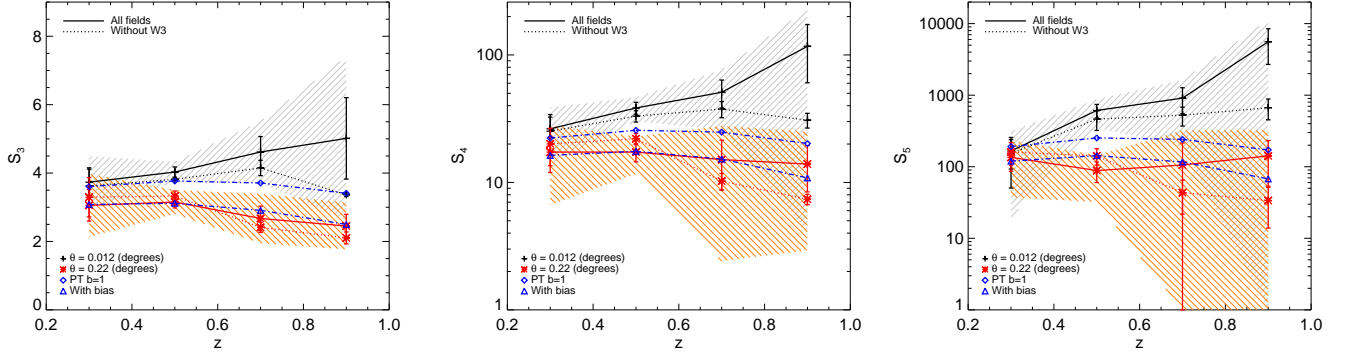
Figure 10. Evolution of S_3, S_4 and S_5 with redshift at non-linear and a weakly non-linear angular scales. The black symbols linked with solid lines and those linked with dotted lines correspond to $\theta = 0.012$ deg for W1+W2+W3+W4 and without W3 respectively. The hashed grey region represent 2σ around the solid black curves. Similarly for $\theta = 0.22$ deg in red. In addition, perturbation theory predictions for the scale $\theta = 0.22$ deg are given in blue with linear bias (diamonds) and without (triangles).
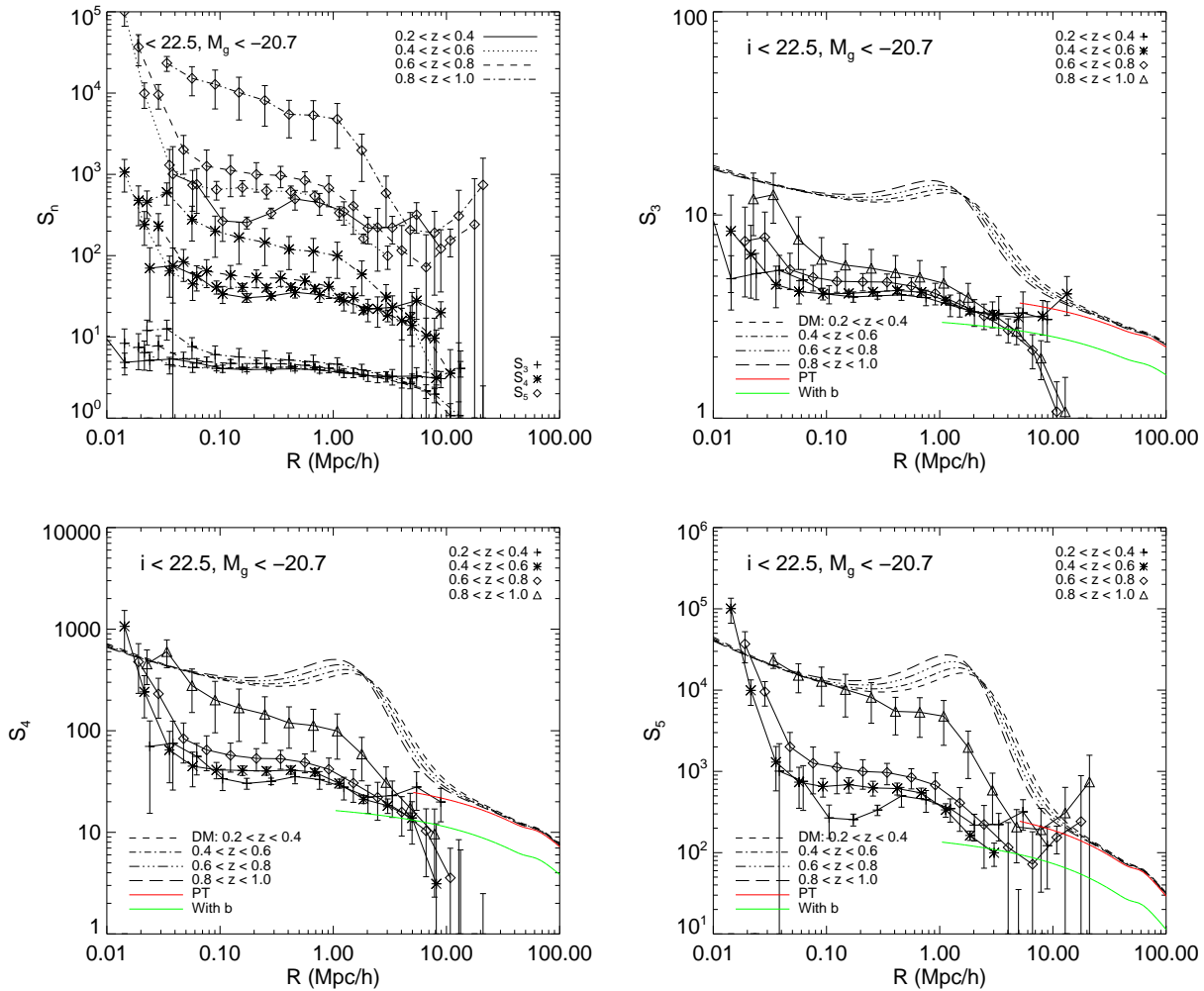
Figure 11. Three-dimensional S_n's in the four redshift bins, together on the same plot (upper left panel) and represented individually (three remaining panels). The dashed and dot-dashed black curves on each panel gives dark matter halo model prediction. The coloured lines represent pure perturbation theory predictions using equations (27), (28) and (29), in two cases: one without bias and one with the most extreme value of linear bias, $b = 1.37$, found in the last redshift bin.

and 11, when simply taking into account effects of linear bias:

$$S_{n,\mathrm{g}} = \frac{S_n}{b^{2(n-2)}}, \qquad (30)$$

with the values of b measured in Section 4.2.3 and given in Table 4.2.3. With such an agreement well within the error bars, we did not fit higher order bias terms (Fry & Gaztanaga 1993); these are clearly consistent with zero at the level of approximation of our measurements.

In addition, on Figure 11, the full halo-model predictions for the dark matter are given using the method of Fry et al. (2011). What is interesting to notice here is that the halo model predictions and measurements are consistent concerning the location of the transition between the weakly non-linear regime and the highly non-linear regime.

5   CONCLUSIONS

We have measured the hierarchical moments of the galaxy distribution S_3, S_4 and S_5 in a volume-limited sample of more than one million galaxies spanning the redshift range $z \sim 1$ to $z \sim 2$. Our measurements were made in the latest release of the CFHTLS wide and cover an effective area of $133\,\mathrm{deg}^2$.

We are able for the first time to make robust measurements of the evolution of the hierarchical moments as functions of redshift within a large range of angular scales. The survey consists of four independent fields, allowing us to estimate the cosmic variance at each bin and angular scale.

Our main results are as follows:

(i) In the redshift bin $0.2 < z < 0.4$ for a sample with the same cut in absolute magnitude, our results are in excellent agreement with the SDSS demonstrating that our survey is a fair sample of the Universe;

(ii) This is confirmed by a comparison of the field to field scatter of the variance of counts in cells and the predicted hierarchical moments with the analytic "cosmic errors" predicted by Szapudi & Colombi (1996); Szapudi et al. (1999);

(iii) The hierarchical moments that we measure show two regimes separated by a transition region: first, a plateau at small scales ($\lesssim 1\,h^{-1}\,\mathrm{Mpc}$) corresponding to the highly non-linear regime, and then the data tend to another lower plateau at large scales ($\gtrsim 7h^{-1}\,\mathrm{Mpc}$) corresponding to the weakly non-linear regime;

(iv) At non-linear scales, the amplitude of the hierarchical moments increase with redshift: however, a more accurate error analysis demonstrates that our results are also consistent with no redshift evolution within 2σ;

(v) In the weakly non-linear regime measurements are fully consistent with the perturbation theory predictions when a linear bias term (measured from our data) is taken into account. Higher-order bias terms corrections (Fry & Gaztanaga 1993) are negligible compared to linear bias given the precision of our measurements;

(vi) The position of the transition between the non-linear and the weakly non-linear regime $1 \lesssim R \lesssim 10\,h^{-1}\,\mathrm{Mpc}$ is fully compatible with halo model predictions.

A robust conclusion concerning the redshift evolution of the hierarchical moments in the non-linear regime, and the corresponding implications for galaxy formation and evolution, is challenging. This is because the richest clusters in our sample can dramatically influence higher order measurements. A complete understanding of this effect will require a detailed modelling of the counts in cells probability using the halo model formalism and taking into account the halo mass of the most massive structure in our survey. This will be the subject of a subsequent work.

REFERENCES

Bardeen J. M., Bond J. R., Kaiser N., Szalay A. S., 1986, ApJ, 304, 15
Bartolo N., Komatsu E., Matarrese S., Riotto A., 2004, Phys.Rev, 402, 103
Baugh C. M. et al., 2004, MNRAS, 351, L44
Baumgart D. J., Fry J. N., 1991, ApJ, 375, 25
Bernardeau F., 1994a, ApJ, 433, 1
Bernardeau F., 1994b, A&A, 291, 697
Bernardeau F., 1996, A&A, 312, 11
Bernardeau F., Colombi S., Gaztañaga E., Scoccimarro R., 2002, Phys. Rep., 367, 1
Bernardeau F., Schaeffer R., 1992, A&A, 255, 1
Bernstein G. M., 1994, ApJ, 424, 569
Blaizot J. et al., 2006, MNRAS, 369, 1009
Bouchet F. R., Strauss M. A., Davis M., Fisher K. B., Yahil A., Huchra J. P., 1993, ApJ, 417, 36
Calzetti D., Armus L., Bohlin R. C., Kinney A. L., Koornneef J., Storchi-Bergmann T., 2000, ApJ, 533, 682
Coleman G. D., Wu C.-C., Weedman D. W., 1980, ApJS, 43, 393
Colless M. et al., 2001, MNRAS, 328, 1039
Colombi S., Bouchet F. R., Schaeffer R., 1994, A&A, 281, 301
Colombi S., Szapudi I., 2001, in Banday A. J., Zaroubi S., Bartelmann M., eds, Mining the Sky. p. 262
Colombi S., Szapudi I., 2012, in prep.
Colombi S., Szapudi I., Jenkins A., Colberg J., 2000, MNRAS, 313, 711
Colombi S., Szapudi I., Szalay A. S., 1998, MNRAS, 296, 253
Cooray A., Sheth R., 2002, Phys. Rep., 372, 1
Coupon J. et al., 2009, A&A, 500, 981
Coupon J. et al., 2012, A&A, 542, A5
Croton D. J. et al., 2004, MNRAS, 352, 1232
Croton D. J., Norberg P., Gaztañaga E., Baugh C. M., 2007, MNRAS, 379, 1562
Davis M., Peebles P. J. E., 1977, ApJS, 34, 425
Fry J. N., 1984, ApJ, 279, 499

Fry J. N., Colombi S., Fosalba P., Balaraman A., Szapudi I., Teyssier R., 2011, MNRAS, 415, 153

Fry J. N., Gaztanaga E., 1993, ApJ, 413, 447

Fry J. N., Peebles P. J. E., 1978, ApJ, 221, 19

Gaztanaga E., 1994, MNRAS, 268, 913

Groth E. J., Peebles P. J. E., 1977, ApJ, 217, 385

Guth A. H., 1981, Phys.Rev.D, 23, 347

Ilbert O. et al., 2006, A&A, 457, 841

Ilbert O. et al., 2005, A&A, 439, 863

Juszkiewicz R., Bouchet F. R., Colombi S., 1993, ApJL, 412, L9

Kaiser N., Stebbins A., 1984, Nature, 310, 391

Kinney A. L., Calzetti D., Bohlin R. C., McQuade K., Storchi-Bergmann T., Schmitt H. R., 1996, ApJ, 467, 38

Kron R. G., 1980, ApJS, 43, 305

Landy S. D., Szalay A. S., 1993, ApJ, 412, 64

Le Fèvre O. et al., 2005, A&A, 439, 845

Limber D. N., 1953, ApJ, 117, 134

Ma C.-P., Fry J. N., 2000, ApJ, 543, 503

Marinoni C. et al., 2008, A&A, 487, 7

Martínez V. J., 2009, in Martínez V. J., Saar E., Martínez-González E., Pons-Bordería M.-J., eds, Lecture Notes in Physics, Berlin Springer Verlag Vol. 665, Data Analysis in Cosmology. pp 269–289

Mo H. J., White S. D. M., 1996, MNRAS, 282, 347

Peacock J. A., Smith R. E., 2000, MNRAS, 318, 1144

Peebles P. J. E., 1980, The large-scale structure of the universe

Politzer H. D., Wise M. B., 1984, ApJL, 285, L1

Regnault N. et al., 2009, A&A, 506, 999

Ross A. J., Brunner R. J., Myers A. D., 2006a, ApJ, 649, 48

Ross A. J., Brunner R. J., Myers A. D., 2006b, ApJ, 649, 48

Ross A. J., Brunner R. J., Myers A. D., 2007, ApJ, 665, 67

Scoccimarro R., Sheth R. K., Hui L., Jain B., 2001, ApJ, 546, 20

Scranton R. et al., 2002, ApJ, 579, 48

Sharp N. A., Bonometto S. A., Lucchin F., 1984, A&A, 130, 79

Szalay A. S., Connolly A. J., Szokoly G. P., 1999, AJ, 117, 68

Szapudi I., Colombi S., 1996, ApJ, 470, 131

Szapudi I., Colombi S., Bernardeau F., 1999, MNRAS, 310, 428

Szapudi I., Postman M., Lauer T. R., Oegerle W., 2001, ApJ, 548, 114

Szapudi I., Szalay A. S., 1993a, ApJ, 414, 493

Szapudi I., Szalay A. S., 1993b, ApJ, 408, 43

Szapudi I., Szalay A. S., Boschan P., 1992, ApJ, 390, 350

APPENDIX A: WEIGHTED STATISTICS

In this Appendix, we describe the way we estimate errors of the combined quantities.

Let x_i, $i = 1, \ldots, n$, be independent variables, $\langle x_i x_j \rangle = \langle x_i \rangle \langle x_j \rangle$ for $i \neq j$, with a common mean $\langle x_i \rangle = \mu$ and variances $\langle (x_i - \mu)^2 \rangle = \sigma_i^2$. Conceptually, the x_i are observations of some quantity in independent fields. Let w_i be a set of weights we define and use to compute a weighted mean

$$\bar{x} \equiv \frac{1}{w_{\text{tot}}} \sum_{i=1}^{n} w_i x_i, \tag{A1}$$

and dispersion

$$\sum_{i=1}^{n} w_i (x_i - \bar{x})^2, \tag{A2}$$

with $w_{\text{tot}} \equiv \sum w_i$. We seek a relation between the dispersion among the samples, Δx, and the uncertainty in the mean, $\Delta \bar{x}$. The expectation of the weighted mean is

$$\langle \bar{x} \rangle = \frac{1}{w_{\text{tot}}} \sum_{i=1}^{n} w_i \langle x_i \rangle = \mu, \tag{A3}$$

and the expectation of the weighted variance is

$$\langle (\Delta x)^2 \rangle = \frac{1}{w_{\text{tot}}} \sum_{i=1}^{n} w_i \langle x_i^2 - 2\bar{x} x_i + \bar{x}^2 \rangle. \tag{A4}$$

The terms in the sum can be expressed in terms of μ and the σ_i^2,

$$\langle x_i^2 \rangle = \mu^2 + \sigma_i^2, \tag{A5}$$

$$\begin{aligned}
\langle \bar{x} x_i \rangle &= \frac{1}{w_{\text{tot}}} \sum_j w_j \langle x_i x_j \rangle \\
&= \frac{1}{w_{\text{tot}}} \left[w_i(\mu^2 + \sigma_i^2) + \sum_{i \neq j} w_j \mu^2 \right] \mu^2 + \frac{w_i \sigma_i^2}{w_{\text{tot}}},
\end{aligned} \tag{A6}$$

and

$$\begin{aligned}
\langle \bar{x}^2 \rangle &= \frac{1}{w_{\text{tot}}^2} \sum_{jk} w_j w_k \langle x_j x_k \rangle \\
&= \frac{1}{w_{\text{tot}}^2} \left[\sum_j w_j^2 (\mu^2 + \sigma_j^2) + \sum_{j \neq k} w_j w_k \mu^2 \right] \\
&= \mu^2 + \frac{1}{w_{\text{tot}}^2} \sum w_j^2 \sigma_j^2. \tag{A7}
\end{aligned}$$

Adding these together, the terms in μ cancel, leaving

$$\begin{aligned}
\langle (\Delta x)^2 \rangle &= \frac{1}{w_{\text{tot}}} \sum_i w_i \left[\sigma_i^2 - \frac{2 w_i \sigma_i^2}{w_{\text{tot}}} + \frac{\sum_j w_j^2 \sigma_j^2}{w_{\text{tot}}^2} \right] \\
&= \frac{1}{w_{\text{tot}}} \sum_i w_i \sigma_i^2 - \frac{1}{w_{\text{tot}}^2} \sum_i w_i^2 \sigma_i^2. \tag{A8}
\end{aligned}$$

The variance in $\bar{x}$ is similarly computed to be

$$\langle (\Delta \bar{x})^2 \rangle = \langle \bar{x}^2 \rangle - \langle \bar{x} \rangle^2 = \frac{1}{w_{\text{tot}}^2} \sum_i w_i^2 \sigma_i^2. \tag{A9}$$

In several cases this leads to a simple relation between Δx and $\Delta \bar{x}$. If all the w_i are equal then

$$\langle (\Delta x)^2 \rangle = \frac{n-1}{n^2} \sum_i \sigma_i^2, \tag{A10}$$

and

$$\langle (\Delta \bar{x})^2 \rangle = \frac{1}{n^2} \sum_i \sigma_i^2. \tag{A11}$$

For $w_i = 1/\sigma_i^2$

$$\langle (\Delta x)^2 \rangle = \frac{n-1}{\sum_i 1/\sigma_i^2} \tag{A12}$$

and

$$\langle (\Delta \bar{x})^2 \rangle = \frac{1}{\sum_i 1/\sigma_i^2}. \tag{A13}$$

The weights $w_i = 1/\sigma_i^2$ are the minimum variance estimator, and choosing the effective area as weights is the best approximation to this.[13] Therefore, we use equation (A1) with weights $w_i = S_{\text{eff},i}$ as the average over fields, and adopt as our estimate of uncertainty

$$\langle (\Delta \bar{x})^2 \rangle = \frac{\langle (\Delta x)^2 \rangle}{n-1}. \tag{A14}$$

APPENDIX B: S_N MEASUREMENTS

---

[13] at least in the Poisson approximation, when $x_i = F_1$ measured in field i

$0.2 < z < 0.4$

θ	S_3	σ_{S_3}	S_4	σ_{S_4}	S_5	σ_{S_5}
0.0011	9.34	4.84	−8.92	3.96	−15.5	7.99
0.0016	4.45	1.33	−4.29	0.80	−6.8	1.85
0.0027	4.72	1.21	54.7	42.7	−84.0	44.7
0.0043	4.90	0.91	58.6	38.3	625	735
0.0070	4.39	0.55	43.6	15.0	468	262
0.0118	3.73	0.38	26.3	6.22	166	73.1
0.0193	3.62	0.21	23.6	2.91	158	26.4
0.0317	3.67	0.14	24.8	1.83	208	30.3
0.0516	3.71	0.22	27.6	4.12	310	84.2
0.0849	3.59	0.31	25.8	5.11	278	83.2
0.1392	3.30	0.40	21.7	5.44	216	68.8
0.2273	3.06	0.46	17.3	5.33	135	48.9
0.3729	2.99	0.65	17.9	7.01	138	51.2
0.6105	3.02	0.81	21.8	8.96	198	80.7
1.0001	2.81	0.63	15.5	5.60	75.7	53.5

$0.4 < z < 0.6$

θ	S_3	σ_{S_3}	S_4	σ_{S_4}	S_5	σ_{S_5}
0.0011	8.18	4.10	1007	435	89701	30529
0.0016	6.27	2.45	228	101	8823	3051
0.0027	4.46	1.03	61.1	32.1	1157	645
0.0043	4.12	0.54	42.3	15.8	656	343
0.0070	4.01	0.27	38.9	7.14	579	150
0.0118	4.03	0.15	38.4	4.11	611	131
0.0193	4.10	0.09	37.9	3.40	557	115
0.0317	4.17	0.14	38.8	3.50	547	91.4
0.0516	4.09	0.13	36.9	2.93	484	70.3
0.0849	3.72	0.12	28.6	2.89	299	56.4
0.1392	3.30	0.10	20.0	1.86	145	18.8
0.2273	3.15	0.17	17.3	2.81	88.5	28.2
0.3729	3.07	0.35	13.1	5.85	−10.1	41.4
0.6105	3.12	0.60	2.94	8.54	−249	43.0
1.0001	4.01	0.87	−5.00	11.4	−595	241

$0.6 < z < 0.8$

θ	S_3	σ_{S_3}	S_4	σ_{S_4}	S_5	σ_{S_5}
0.0011	7.32	3.43	455	232	33737	13985
0.0016	7.64	2.53	220	93.4	8710	2910
0.0027	5.30	1.08	79.8	33.9	1832	916
0.0043	4.86	0.70	61.8	23.2	1151	668
0.0070	4.64	0.54	54.7	17.4	1025	541
0.0118	4.62	0.45	51.0	12.6	910	360
0.0193	4.60	0.44	50.6	10.7	885	260
0.0317	4.40	0.44	46.6	9.81	769	214
0.0516	4.05	0.49	40.0	11.5	620	255
0.0849	3.58	0.48	29.1	10.3	373	206
0.1392	3.13	0.45	21.1	8.56	203	144
0.2273	2.67	0.36	15.1	6.34	106	108
0.3729	2.13	0.41	9.87	6.38	65.7	99
0.6105	1.06	0.43	3.41	3.25	141	53
1.0001	−0.69	0.33	−5.60	2.64	221	588

$0.8 < z < 1.0$

θ	S_3	σ_{S_3}	S_4	σ_{S_4}	S_5	σ_{S_5}
0.0011	11.0	3.75	365	136	−819	226
0.0016	11.5	3.18	483	147	16011	3325
0.0027	6.96	2.01	223	102	10415	4062
0.0043	5.54	1.55	161	84.7	8770	4397
0.0070	5.20	1.41	135	71.8	6970	3767
0.0118	5.01	1.19	117	56.4	5579	2893
0.0193	4.77	1.02	96.0	42.0	3757	1829
0.0317	4.54	0.93	90.5	40.2	3664	1865
0.0516	4.23	0.85	79.9	37.7	3271	1836
0.0849	3.60	0.62	47.5	21.7	1352	792
0.1392	2.99	0.44	24.9	10.5	403	249
0.2273	2.45	0.34	13.9	5.50	142	90.5
0.3729	1.81	0.39	7.74	5.89	131	109
0.6105	0.99	0.47	−1.92	8.71	211	225
1.0001	−0.36	0.95	−15.02	17.0	508	575

Table B1. Measured S_n and their error bars in the bins $0.2 < z < 0.4$, $0.4 < z < 0.6$, $0.6 < z < 0.8$ and $0.8 < z < 1$, respectively on the upper left, upper right, bottom left and bottom right table. On each table, the first column refers to the angular size of the square cells used to perform the measurements. The next columns display successively S_3 and its error bars, S_4 and its error bars and S_5 and its error bars. The counts in cells method used to perform the measurements is described in § 3.3. The way the four fields are combined and the corresponding error bars are computed is detailed in 3.4.